ADVANCED FUNCTIONAL MATERIALS
www.afm-journal.de

Optimizing Local Configuration of Interphase Copper Oxide by Ru Atoms Incorporation for High-Efficient Nitrate Reduction to Ammonia

Yunxiang Lin, Ying Wang, Ying Xu, Hengjie Liu, Xue Liu, Lei Shan, Chuanqiang Wu, Li Yang,* and Li Song**

The electrochemical reduction of nitrate offers an environmentally friendly and sustainable development strategy to mitigate nitrate pollution and further facilitate value-added ammonia synthesis. Here, interphase $Cu_{2+1}O$ (regarded as Cu_2O with metal excess defects) featured by abundant Cu^0 and $Cu^{\delta+}$ sites with Ru single atoms incorporation (marked as $Ru_{SA}@Cu_{2+1}O$) are synthesized by fast Joule heating method for efficient nitrate reduction to ammonia. The X-ray absorption spectroscopy found that the incorporation of Ru atoms can effectively tune the local electronic structure of $Cu_{2+1}O$ substrate with charge polarization. The as-prepared $Ru_{SA}@Cu_{2+1}O$ exhibits a remarkable Faradaic efficiency (FE) of 98.02% and an ammonia yield of 0.81 mmol h^{-1} cm^{-2} at the potential of -0.4 V (vs RHE). In situ, attenuated total reflection surface-enhanced infrared absorption spectroscopy and theoretical investigations further confirm that Ru incorporation promotes the rapid transfer of the hydrogenation process. This study not only presents a feasible approach for fabricating interphase catalysts through fast Joule heating synthesis, but also offers insights into effectively regulating the local electronic structure of electrocatalysts for boosted reaction process.

1. Introduction

Electrochemical nitrate (NO_3^-) reduction reaction (NO_3RR) has been widely studied due to its significant importance in wastewater treatment and clean energy conversion.[1–4] Considering the energy consumption and operating simplicity, electrochemical NO_3RR is a promising candidate for the replacement of the Haber-Bosch method, which requires high temperature, high pressure, and excessive energy consumption along with greenhouse gas emissions.[5,6] Although the co-reduction of N_2 and H_2O to produce NH_3 under ambient conditions has been studied in recent years, the high bond energy of the nonpolar N≡N bond (941 kJ mol^{-1}) caused a high energy requirement. Besides, the low solubility of N_2 in electrolytes also leads to the inevitable competition hydrogen evolution reaction (HER) under high reduction potential. Nevertheless, the NO_3RR is an intricate process that contains eight electrons transferred along with various intermediates, which is distinctly restricted by a high energy barrier and the competing HER.[7,8] As such, effective catalytic configurations with the favorable adsorption of intermediates (e.g., $^*NO_2$, $^*NO$) and boosted reaction kinetics are key aspects that significantly influence the overall performance of NO_3RR.[9–11] Altering the adsorption of key intermediates could not only reduce the energy barrier, but also offer the opportunity to understand the reaction mechanism associated with the reaction pathways. Considering that the adsorption of intermediates is mainly influenced by the local configuration of the catalysts, which play the key role in the subsequent reaction process. Hence, designing highly efficient electrocatalysts with optimized local configuration and electronic structure has been a hot topic in recent years.[12–15]

As is widely reported that transition metal (e.g., Cu, Co, and Ru) based electrocatalysts displayed ideal NO_3RR performance owing to the unfilled d-orbital electrons and tunable d-band structure, which plays a significant influence on the activation and hydrogenation of NO_3^-.[16–23] Considering that the NO_3RR is a hydrogenation reaction that consumes protons from H_2O dissociation in alkaline conditions, balancing the proton supply and NO_3^-

Y. Lin, Y. Wang, Y. Xu, X. Liu, L. Shan, C. Wu, L. Yang
Institutes of Physical Science and Information Technology
Leibniz International Joint Research Center of Materials Sciences
Information Materials and Intelligent Sensing Laboratory of Anhui Province
Center of Free Electron Laser & High Magnetic Field, School of Chemistry & Chemical Engineering
Anhui University
Hefei 230601, China
E-mail: wucq@ahu.edu.cn; yangli91@mai.ustc.edu.cn
H. Liu, L. Song
National Synchrotron Radiation Laboratory
University of Science and Technology of China
Hefei 230029, China
E-mail: song2012@ustc.edu.cn
L. Song
Zhejiang Institute of Photonelectronics
Jinhua, Zhejiang 321004, China

The ORCID identification number(s) for the author(s) of this article can be found under https://doi.org/10.1002/adfm.202417486

DOI: 10.1002/adfm.202417486

hydrogenation process is an important thing regarding such a so-called proton coupling electron transfer process.[24–26] Among various transition metals, Cu-based catalysts exhibit excellent activity in NO_3^- adsorption and hydrogenation along with a low-cost and high structural tunability. But the adsorption of intermediates (e.g., $^*NO_2^-$, $^*NO$) on pure Cu catalyst is strong, leading to the undesired accumulation of intermediates and decelerating the reaction process.[27,28] Besides, introducing main-group metals can suppress the competing HER due to the weakened affinity of protons.[29] Besides, Cu atom incorporation into the vacancy of $Co_{0.85}Se$ can significantly promote the electron transfer from Cu to Co sites via bridging bonds, leading to an electron-deficient state of Cu, thus accelerating the dissociation of NO_3^- and stabilization of NO_2^-.[30] Most recently, the vacancies in the copper oxides can regulate the local energy levels, promote nitrate adsorption, and enhance water dissociations, which displayed significantly accelerated reaction kinetics.[31–33] Therefore, the speculation that optimizing the local configuration of Cu-based catalyst can significantly promote the NO_3RR performance could be rationally expected.

In this work, interphase $Cu_{2+1}O$ featured abundant Cu^0 and $Cu^{\delta+}$ sites and Ru single atoms incorporation ($Ru_{SA}@Cu_{2+1}O$) was successfully synthesized by fast Joule heating methods for high-efficient NO_3RR. Notably, the $Ru_{SA}@Cu_{2+1}O$ presented a high Faradaic efficiency (FE) of 98.02% and ammonia yield of 0.81 mmol h^{-1} cm^{-2} at -0.4 V versus RHE, exceeding that of $Cu_{2+1}O$ (FE_{max} of 61.14% and 0.27 mmol h^{-1} cm^{-2}) with an ideal stability. Synchrotron radiation-based X-ray absorption fine structure (XAFS) demonstrated that the incorporation of Ru atoms into $Cu_{2+1}O$ catalyst could modulate the local geometric configuration Cu with a favorable electronic structure. Subsequent attenuated total reflection surface-enhanced infrared absorption spectroscopy (ATR-SEIRAS) and theoretical analysis further confirmed the role of Ru incorporation in promoting the reaction intermediates transfer and hydrogenation. This work proposed a feasible approach for the fabrication of an efficient catalyst with the fine-tuned local structure and optimized adsorption of intermediates.

2. Results and Discussion

2.1. Synthesis and Characterization of $Cu_{2+1}O$ and $Ru_{SA}@Cu_{2+1}O$

The $Cu_{2+1}O$, regarded as a form of Cu_2O with metal excess defects, is one type of copper oxide that includes both Cu^0 and $Cu^{\delta+}$ species, which can serve as the synthetic active sites. Owing to its unique interphase, there is a lack of literature focused on synthesizing pure interphase $Cu_{2+1}O$ nanomaterials. Owing to the ultrafast heating and cooling rates, fast Joule heating synthesis offers an exceptional platform for the synthesis of interphase nanomaterials. As illustrated in **Figure 1a**, the precursors were first prepared by using a simple co-reduction of Cu and Ru salts by using sodium borohydride as a reducing agent. Followed by fast Joule heating treatment, the interphase $Cu_{2+1}O$ and $Ru_{SA}@Cu_{2+1}O$ were successfully synthesized and applied for further electrocatalytic process. As depicted in the Figure 1b, the X-ray diffraction (XRD) patterns of $Cu_{2+1}O$ and $Ru_{SA}@Cu_{2+1}O$ show a series diffraction peak at 29.5°, 36.4°, 42.3°, 61.3°and 73.5° which are well indexed to (110), (111), (200), (220) and (311) of planes of $Cu_{2+1}O$ (JCPDS No. 05–0667). The similar diffraction features of $Cu_{2+1}O$ and $Ru_{SA}@Cu_{2+1}O$ indicate that the incorporation of Ru atoms doesn't influence the fast Joule heating synthesis of interphase $Cu_{2+1}O$. It deserves to be emphasized that the signal-to-noise ratio of the XRD pattern for the $Ru_{SA}@Cu_{2+1}O$ is lower than that of $Cu_{2+1}O$, which may due to the generalized amorphous structure in the $Ru_{SA}@Cu_{2+1}O$ induced by Ru incorporation. In comparison, when the precursor was treated in a traditional tubular furnace with slower rising and cooling rates, the obtained material mainly displayed the crystal structure of $Cu_{2+1}O$ and CuO (Figure S1, Supporting Information), indicating that the fast Joule heating methods could contribute to the successful synthesis of pure interphase $Cu_{2+1}O$. Then, the transmission electron microscope (TEM) images of as-prepared samples were collected to investigate the morphology and structure. As shown in Figure 1c and Figure S2a (Supporting Information), the $Ru_{SA}@Cu_{2+1}O$ and $Cu_{2+1}O$ exhibit uniformly gathered nanoparticles. Furthermore, the high-resolution TEM (HRTEM) image of $Ru_{SA}@Cu_{2+1}O$ clearly displays continuous lattice fringes with a lattice spacing of 2.46 and 2.13 Å, corresponding to the (111) and (200) planes (Figure 1d). It could be observed that some part of the nanoparticles exhibits the lattice fringe with a larger spacing of 2.48 Å, potentially due to lattice expansion induced by Ru atom incorporation. Additionally, some of the amorphous zones could be detected in the $Ru_{SA}@Cu_{2+1}O$ rather than $Cu_{2+1}O$ (Figure S2b; Figure S3, Supporting Information), which is consistent with the XRD results and may due to the incorporation of Ru atoms can influence the crystal growth during the ultra-fast synthetic process. Through high-angle annular dark-field scanning transmission electron microscopy (HAADF-STEM), it is evident from Figure 1e that the bright dots could be observed on the $Cu_{2+1}O$ substrate, further confirming the successful incorporation of Ru single atoms. The elemental mapping image collected from energy-dispersive X-ray analysis (EDS) shows that Cu, O, and Ru are uniformly distributed in $Ru_{SA}@Cu_{2+1}O$ (Figure 1f). In comparison, the $Cu_{2+1}O$ exhibits a uniform distribution of Cu and O elements could also be observed, which indicates the successful preparation of the $Cu_{2+1}O$ (Figure S4, Supporting Information). Additionally, the Ru amount was measured as 2.4 wt% by inductively coupled plasma mass spectrometry.

The chemical states of Cu, O, and Ru were further detected by the X-ray photoelectron spectroscopy (XPS) measurements. As for the valence states of Cu displayed in Figure 1g, the peaks located ≈931.3 and 951.28 eV can be assigned to the $2p_{3/2}$ and $2p_{1/2}$ of $Cu^{\delta+}$ that originate from Cu^0 and Cu^+ species, respectively. Furthermore, the scattering peaks around the binding energies of 933.8 and 953.8 eV are attributed to the $2p_{3/2}$ and $2p_{1/2}$ of Cu^{2+}. The Cu LMM Auger spectra of $Ru_{SA}@Cu_{2+1}O$ and $Cu_{2+1}O$ also demonstrated that the incorporation of Ru regulated the local valence states of Cu (Figure S5, Supporting Information). The relative contents of Cu^0 and Cu^+ were also analyzed from XPS fitting results to clarify the valence states of copper species. The Cu^0 to Cu^+ ratio is 0.42 for $Ru_{SA}@Cu_{2+1}O$ and 0.33 for $Cu_{2+1}O$, indicating the successful regulation of the local electronic structure. Besides, we can also find that the Cu^{2+} to $Cu^{\delta+}$ ratios are 1.06 and 1.85 for $Cu_{2+1}O$ and $Ru_{SA}@Cu_{2+1}O$, indicating that the incorporation of Ru atoms can significantly promote charge

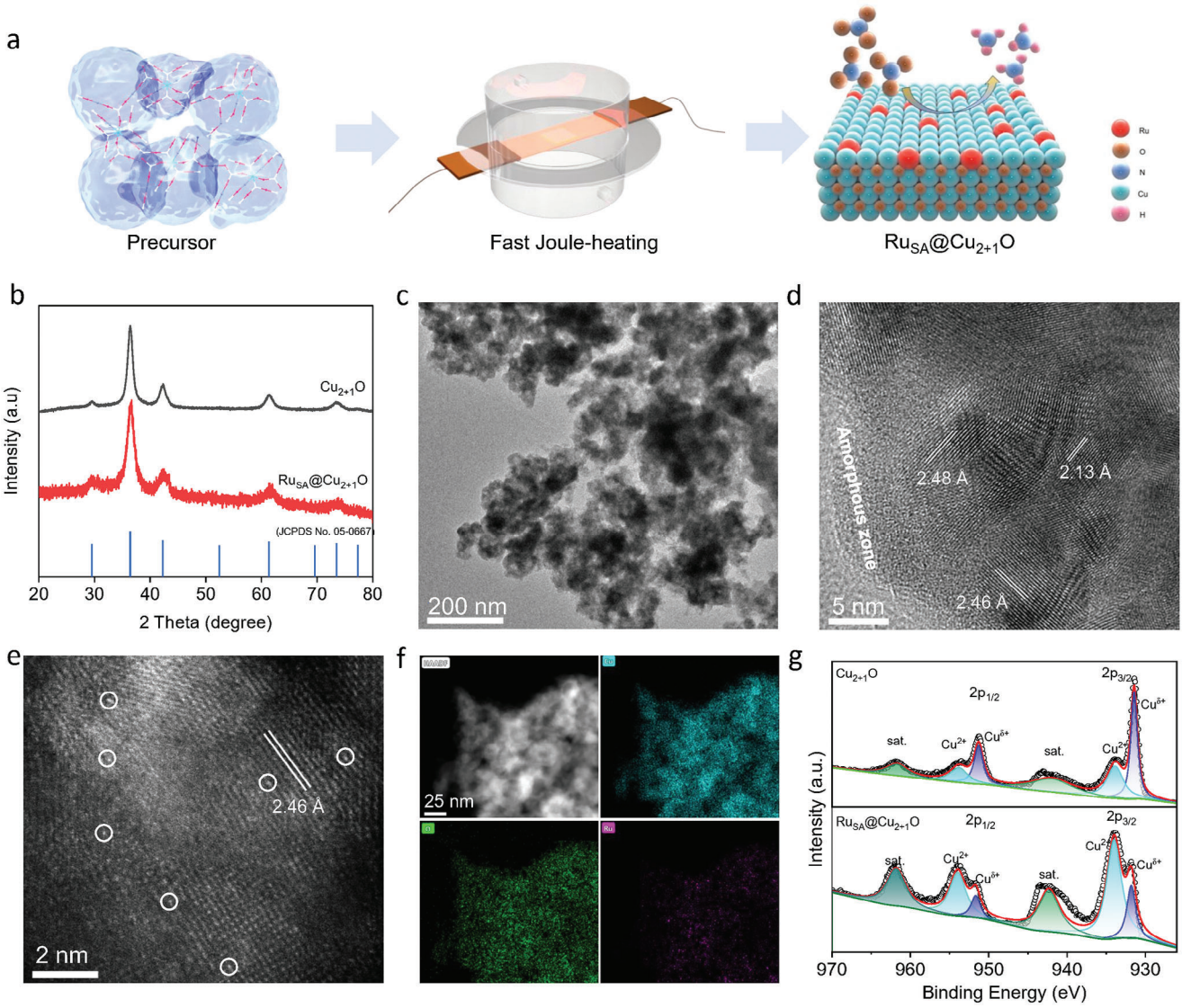

Figure 1. Morphology and microstructural characterization of $Cu_{2+1}O$ and $Ru_{SA}@Cu_{2+1}O$. a) Illustration of the synthetic procedure. b) XRD patterns of $Ru_{SA}@Cu_{2+1}O$ and $Cu_{2+1}O$, c) TEM, and d) HRTEM images of $Ru_{SA}@Cu_{2+1}O$. e) HAADF-STEM image of $Ru_{SA}@Cu_{2+1}O$ and f) Elemental mapping of $Ru_{SA}@Cu_{2+1}O$. g) Cu 2p XPS spectra of $Ru_{SA}@Cu_{2+1}O$ and $Cu_{2+1}O$.

polarizations. The two separate peaks around binding energies of 467.4 and 488.4 eV are ascribed to the $3p_{3/2}$ and $3p_{1/2}$ scattering peaks of Ru^{4+} valence state, which may be originated from the coordination of Ru and adjacent O atoms (Figure S6a, Supporting Information).[34] In addition, the lattice oxygen and oxygen vacancy could also be observed in the O 1s XPS spectra at the bind energies ≈530.9 and 532.5 eV, respectively (Figure S6b, Supporting Information).[35]

In order to further confirm the electronic structure of Cu regulated by the Ru incorporation, we conducted synchrotron radiation X-ray absorption spectroscopies. The Cu *L*-edge X-ray absorption near edge structure (XANES) of $Cu_{2+1}O$ and $Ru_{SA}@Cu_{2+1}O$ was first measured to investigate the local electronic structure of Cu. As shown in **Figure** 2a, the peak intensity of L_3-edge for $Ru_{SA}@Cu_{2+1}O$ is lower than that of $Cu_{2+1}O$, indicating more electrons occupied in the 3d orbital for $Ru_{SA}@Cu_{2+1}O$. Besides, this charge polarization between Ru and substrate can also be observed in the O *K*-edge XANES spectra with rearranged peak intensities of σ^* and π^* bonds (Figure 2b). Additionally, the Cu *K*-edge X-ray absorption fine structure (XAFS) was also conducted to analyze the fine local structure of Cu. As shown in Figure 2c, the $Ru_{SA}@Cu_{2+1}O$ and $Cu_{2+1}O$ exhibit similar XANES spectra to that of Cu_2O rather than that of CuO and Cu, which can be attributed to their similar local geometric features. Besides, the $Ru_{SA}@Cu_{2+1}O$ displayed the lowest pre-edge peak while the highest white-line peak, implying the incorporation of Ru atoms into the $Cu_{2+1}O$ substrate along with significant charge polarization. The first derivate XANES spectra again confirm that the Cu absorption edge in both $Cu_{2+1}O$ (8984.28 eV) and $Ru_{SA}@Cu_{2+1}O$ (8984.46 eV) is higher than that of Cu foil (8982.97 eV), lower than CuO (8986.26 eV), and close to Cu_2O (8984.70 eV), indicating that the

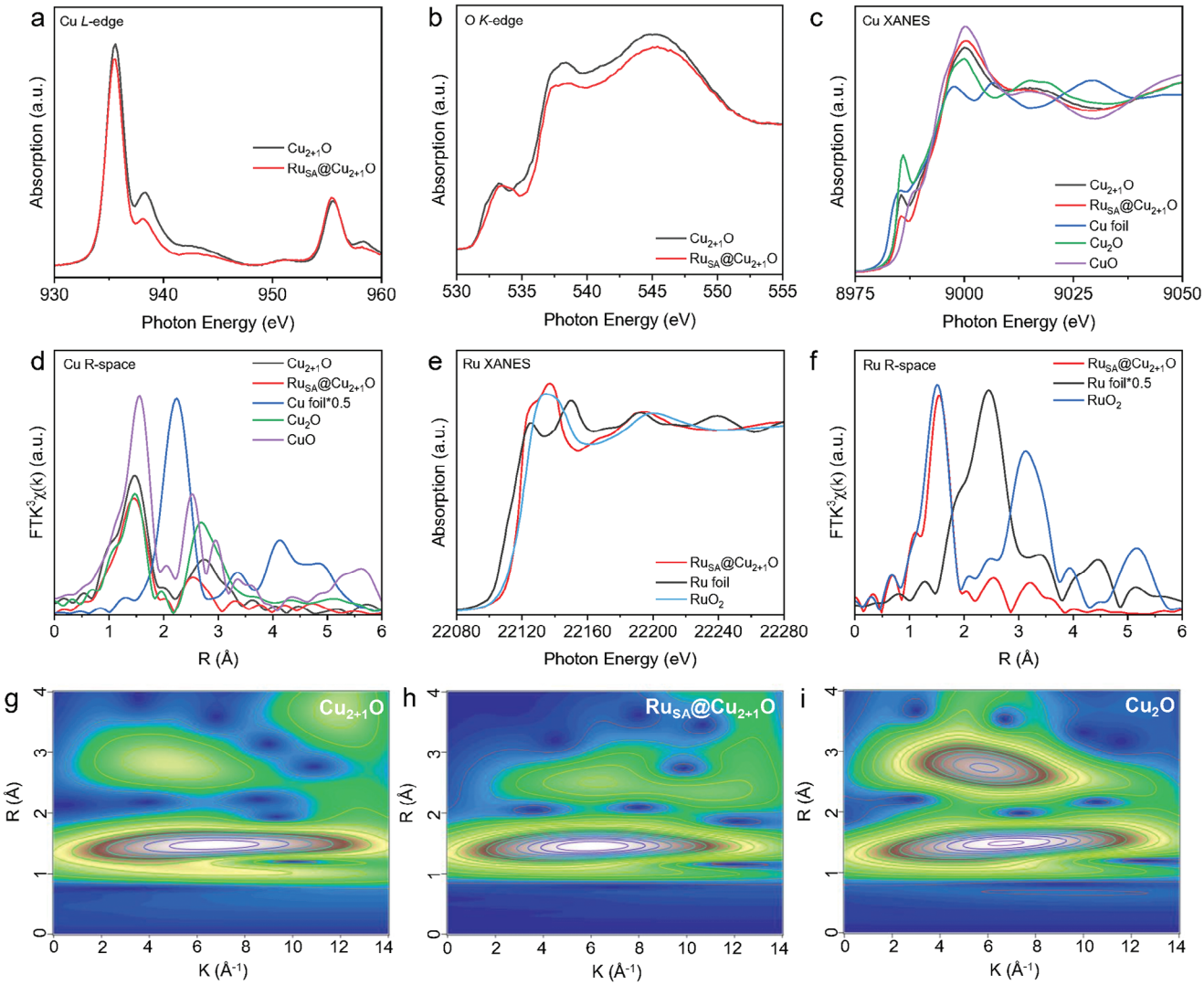

Figure 2. Electronic structure characterizations. a) Cu *L*-edge, b) O *K*-edge, and c) Cu *K*-edge XANES spectra of the as-prepared $Ru_{SA}@Cu_{2+1}O$ and counterparts. d) FT-EXAFS curves at the R-space of the Cu *K*-edge for the $Ru_{SA}@Cu_{2+1}O$, $Cu_{2+1}O$, and other copper oxide counterparts. e) Ru *K*-edge XANES spectra of the as-prepared $Ru_{SA}@Cu_{2+1}O$, Ru foil, and RuO_2. f) FT-EXAFS curves of the Ru *K*-edge at R-space for the as-prepared $Ru_{SA}@Cu_{2+1}O$ and counterparts. g–i) WT-EXAFS curves of the Cu *K*-edge EXAFS curves for $Cu_{2+1}O$, $Ru_{SA}@Cu_{2+1}O$, Cu_2O.

valence state is primarily monovalent (Figure S7, Supporting Information). The Fourier transform extends XAFS (FT-EXAFS) curves of the as-prepared samples in R space and also implies the local configuration of Cu (Figure 2d). The scattering peak located around 1.5 Å can be attributed to the Cu-O bond, while the scattering peak at 2.5 Å originates from the Cu—Cu bond. We can see that the Cu—O bond length of $Ru_{SA}@Cu_{2+1}O$ is slightly lower than that of $Cu_{2+1}O$, which may be attributed to the lattice distortion owing to Ru incorporation. Besides, the shortened bond length can also be observed in the Cu—Cu bond. The EXAFS fitting results also demonstrated that Ru incorporation leads to the rearrangement of the local environment (Figure S8, Table S1, Supporting Information). In detail, the coordination number of Cu—O is 2.26 for $Ru_{SA}@Cu_{2+1}O$ and 2.41 for $Cu_{2+1}O$, confirming the lattice distortion of the Cu—O unit induced by the Ru incorporation. Besides, both the bond length and coordination number of the Cu—Cu bond for $Ru_{SA}@Cu_{2+1}O$ are smaller than those of $Cu_{2+1}O$, which is also consistent with the aforementioned discussions. As for the local structure of Ru, the XANES spectrum of $Ru_{SA}@Cu_{2+1}O$ displays a similar adsorption edge to RuO_2 with a slight shift, implying 4+ valence states of Ru along with slight charge polarization (Figure 2e). Besides, only the Ru—O bond in the FT-EXAFS curve of $Ru_{SA}@Cu_{2+1}O$ at 1.48 Å (without phase correction) further indicates the isolated dispersion of Ru atoms. The EXAFS fitting results also demonstrated the six-coordination environment of the Ru—O bond (Figure S9, Table S2, Supporting Information). In addition, the wavelet-transform EXAFS (WT-EXAFS) of the Cu K-edge EXAFS curves for $Ru_{SA}@Cu_{2+1}O$ exhibit two maximum, attributing to the Cu—O and Cu—Cu bond (Figure 2g–i). The shift of maximum value further indicates the rearrangement of the local environment induced by the Ru atoms incorporation. Hence, the X-ray spectroscopies clearly

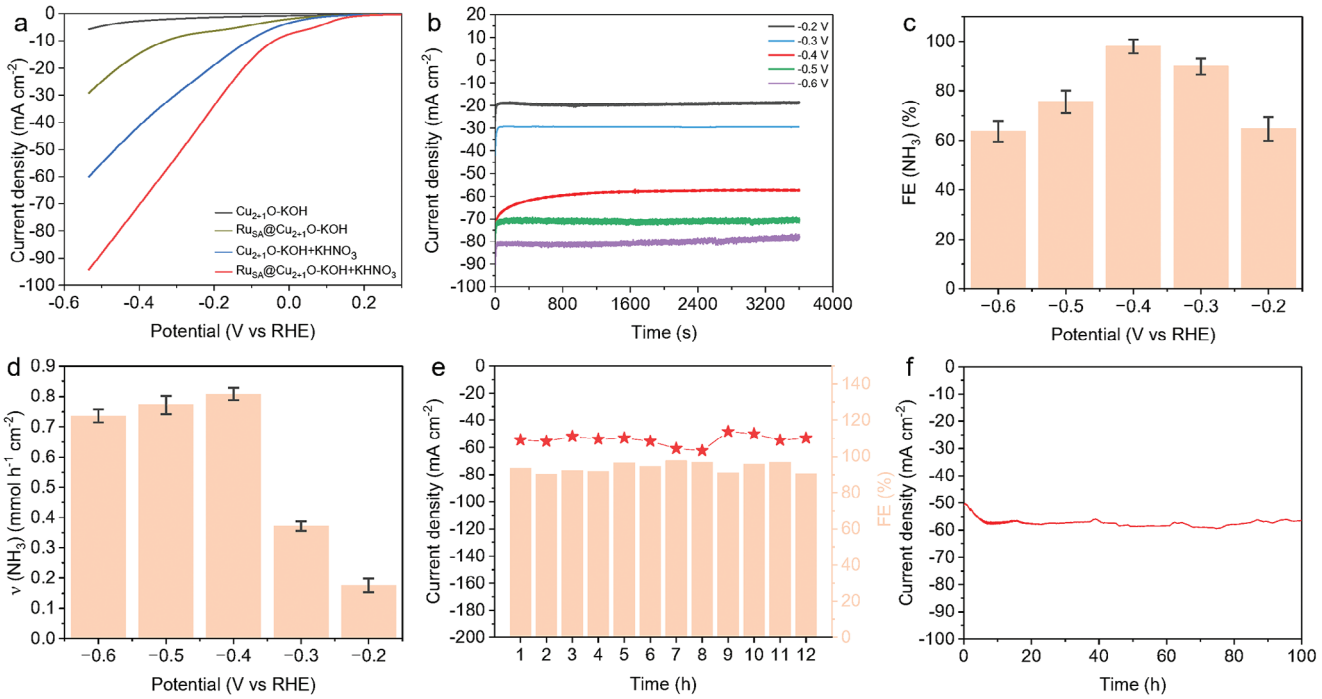

Figure 3. The electrocatalytic activity for NO_3RR. a) LSV curves of $Cu_{2+1}O$ and $Ru_{SA}@Cu_{2+1}O$ in 0.1 M KOH electrolyte with and without 0.1 M KNO_3. b) *I–t*-tests for $Ru_{SA}@Cu_{2+1}O$ at the potential range from −0.2 to −0.6 V (vs RHE) for 1 h. The corresponding c) FEs and d) yields of NH_3 at the different operation potentials. f) Stability test for $Ru_{SA}@Cu_{2+1}O$ under flow cell test.

demonstrated that the introduction of Ru atoms into the $Cu_{2+1}O$ can significantly regulate the local electronic structure of the $Cu_{2+1}O$ substrate, which may help to promote the catalytic performance toward NO_3RR.

2.2. Evaluation of NO_3RR Performance

Considering that the Ru incorporation has directly regulated the local electronic structure of $Cu_{2+1}O$, which may contribute to the electrochemical NO_3^- to ammonia conversion. As shown in **Figure** 3a, the linear sweep voltammetry (LSV) curves were first collected to evaluate the NO_3RR performance of $Cu_{2+1}O$ and $Ru_{SA}@Cu_{2+1}O$ catalysts in 0.1 M KOH with and without adding 0.1 M KNO_3 electrolyte. Generally, the current densities of both samples notably increase after adding NO^{3-}, and the current density of $Ru_{SA}@Cu_{2+1}O$ particularly higher than that of $Cu_{2+1}O$ with a maximum current density of 95 mA cm^{-2}. Meanwhile, the $Ru_{SA}@Cu_{2+1}O$ requires a lower potential to achieve the same current density than that of $Cu_{2+1}O$, indicating the better NO_3RR performance of $Ru_{SA}@Cu_{2+1}O$. It should be noted that the incorporation of Ru atoms could also promote the HER performance, in which the current densities are larger than that without Ru incorporation, which may be due to the regulated local electronic structures. In the subsequent NO_3RR process, the enhanced hydrogen generation may also promote the hydrogenation process and facilitate the reaction kinetics.[31] The NH_3 yield and Faradaic efficiency (FE) were also qualified under a one-hour chronoamperometry (I-t) test (Figure 3b; Figures S10 and S11, Supporting Information). As shown in Figure 3c, the FEs of $Ru_{SA}@Cu_{2+1}O$ reach 98.02% along with an ammonia yield of 0.81 mmol h^{-1} cm^{-2} at the potential of −0.4 V, which is comparable to recent literature (Table S3, Supporting Information). It could be observed that although the FEs at −0.2 and −0.3 V are higher than those of −0.5 and −0.6 V (Figure 3d), the ammonia yields are significantly lower, which is mainly because of the larger partial current densities of ammonia generation at –0.5 and –0.6 V. In comparison, both the maximum FE (61.14%) and NH_3 yield (0.27 mmol h^{-1} cm^{-2}) at the operation potentials for $Cu_{2+1}O$ are lower than those of $Ru_{SA}@Cu_{2+1}O$ (Figure S12, Supporting Information). The main by-product of NO_2^- was also determined by UV–vis spectroscopy by comparing the absorption strength to the standard curve (Figure S13, Supporting Information). It should be noted that there are no obvious NO_2^- was detected under various potentials, indicating the high selectivity of $Ru_{SA}@Cu_{2+1}O$ toward ammonia. The NO_3RR performance of $Ru_{SA}@Cu_{2+1}O$ was also measured under the NO_3^- concentration of 0.05 M and 0.5 M. The current densities show positive correlations with the NO_3^- concentration, in which the higher NO_3^- concentration leads to the larger current density. Besides, the $Ru_{SA}@Cu_{2+1}O$ also shows favorable FEs under various applied potentials with the NO_3^- concentration of 0.05 and 0.5 M, further confirming the high activity toward NO_3RR (Figures S14 and S15, Supporting Information). The electrochemical surface area (ECSA) estimated by double layer capacitance (C_{dl}) value of $Ru_{SA}@Cu_{2+1}O$ is 0.74 mF cm^{-2}, which is twice that of $Cu_{2+1}O$ (0.34 mF cm^{-2}). The larger C_{dl} value of $Ru_{SA}@Cu_{2+1}O$ further indicates that the incorporation of Ru atoms into $Cu_{2+1}O$ substrate significantly increases the accessible active sites (Figure S16,

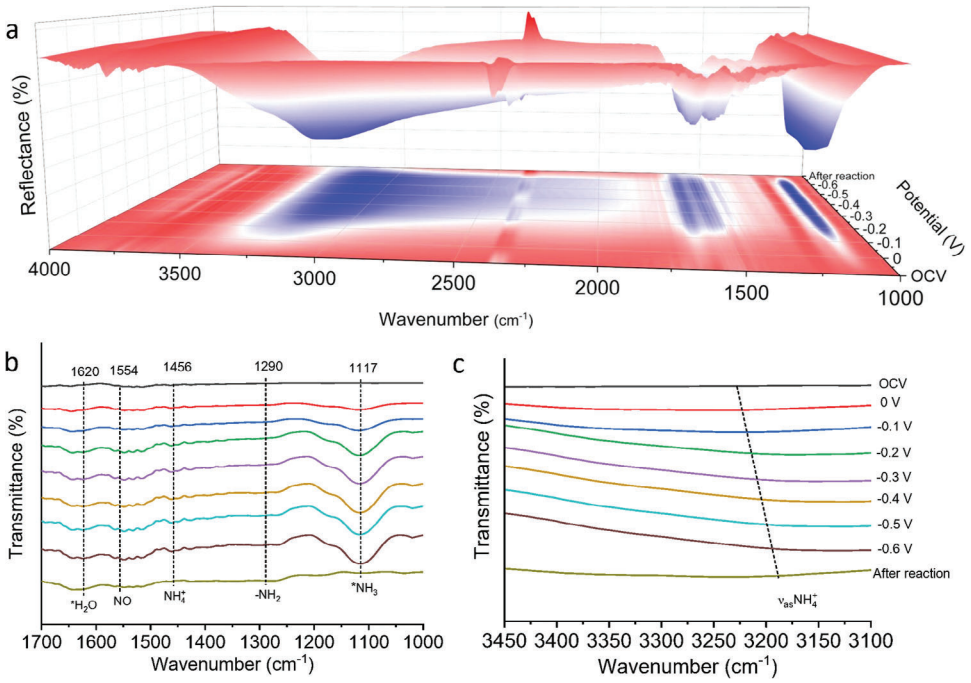

Figure 4. Operando Synchrotron radiation ATR-SEIRAS measurements under various potentials for $Ru_{SA}@Cu_{2+1}O$ during NO_3RR. a) 3D FTIR spectra and corresponding contour maps in the range of 4000 to 1000 cm^{-1}, measured under potentials from 0 to −0.6 V versus RHE and OCV. b) Infrared signals in the range of 1700 to 1000 cm^{-1}. c) Infrared signals in the range of 3450 to 3100 cm^{-1}.

Supporting Information).[36] In order to further investigate the charge transfer, electrochemical impedance spectroscopy (EIS) was conducted. As shown in Figure S17 and Table S4 (Supporting Information), the $Ru_{SA}@Cu_{2+1}O$ exhibits a smaller charge transfer resistance (R_{ct}) than $Cu_{2+1}O$, indicating the fast charge transfer kinetics. Hence, we can conclude from the electrocatalytic NO_3RR performance of $Ru_{SA}@Cu_{2+1}O$ that although incorporation of Ru atoms can promote the HER to a certain extent, and thus facilitates the hydrogenation of intermediates to form ammonia. To further verify the stability of $Ru_{SA}@Cu_{2+1}O$, it was measured by chronoamperometry at the fixed potential of −0.4 V for 12 cycles. As shown in Figure 3e, the current densities can be basically maintained within a narrow range and the relative FE consistently exceeds 90% during the stability test, indicating that the $Ru_{SA}@Cu_{2+1}O$ catalyst has good stability and activity. Besides, the long-term stability test of $Ru_{SA}@Cu_{2+1}O$ was conducted for 100 h at the flow cell, which maintained a stable current density without significant attenuations (Figure 3f). It should be noted that the current density dropped at the initial hours during the stability test could be attributed to the inevitable structural evolution under reduction potential, which would be discussed in the following discussions. This consistent performance indicates the excellent stability of the sample under the applied conditions. In order to confirm that the ammonia was generated from the NO_3^- after electrochemical reduction, isotopic labeling experiments were conducted. As shown in Figure S18 (Supporting Information), three peaks were located at 6.16, 6.81, and 7.47 ppm when the nitrogen source was $^{14}NO_3^-$, while double peaks of $^{15}NH_4^+$ were located at 6.46 and 7.38 ppm when the $^{15}NO_3^-$ was used as the nitrogen source from ^1H NMR measurements, indicating that the produced ammonia is origin from NO_3^-. The electrocatalysts after NO_3RR were also analyzed to investigate the structural evolution during electrolysis. As shown in Figure S19 (Supporting Information), the XRD pattern of $Ru_{SA}@Cu_{2+1}O$ displayed the $Cu_{2+1}O$ and Cu species, indicating the inevitable reduction of Cu species under reduction potential. In addition, the TEM image of $Ru_{SA}@Cu_{2+1}O$ after electrolysis exhibits similar features compared to that before electrolysis. Besides, the continuous lattice fringes with the distance of 2.46 and 2.10 Å in the HRTEM image demonstrate the existence of residual interphase $Cu_{2+1}O$ and new generalized Cu (Figure S20, Supporting Information). Furthermore, the XPS spectrum of Cu 2p after electrolysis also shows a higher scattering peak of $Cu^{\delta+}$ species, demonstrating the reduction of high valence states of Cu species (Figure S21, Supporting Information).

The synchrotron radiation attenuated total reflection surface-enhanced infrared absorption spectroscopy (ATR-SEIRAS) was then performed to investigate the reaction pathway of NO_3RR (**Figure 4a**; Figure S22a, Supporting Information). A series of peaks of different intermediates raised with the reducing potential increase from 0 to −0.6 V could be observed. As shown in Figure 4b, the peaks of $-NH_2$ and NH+ 4 located at 1290 and 1456 cm^{-1} clearly demonstrated the formation of ammonia.[37,38] Besides, a faint peak corresponding to the NO characteristic appears at 1554 cm^{-1}, which is the key intermediate of NH_3.[39] Meanwhile, the peak attributed to $^*H_2O$ at 1620 cm^{-1} is associated with the shear bending vibration in the O—H bond plane. The peak at 1117 cm^{-1}, attributed to $^*NH_3$, is generated by the H—N stretching vibration.[1] Furthermore, the wide peak around 3100 cm^{-1} can also be observed due to the formation of NH_4^+, implying the formation of the final product (Figure 4c).

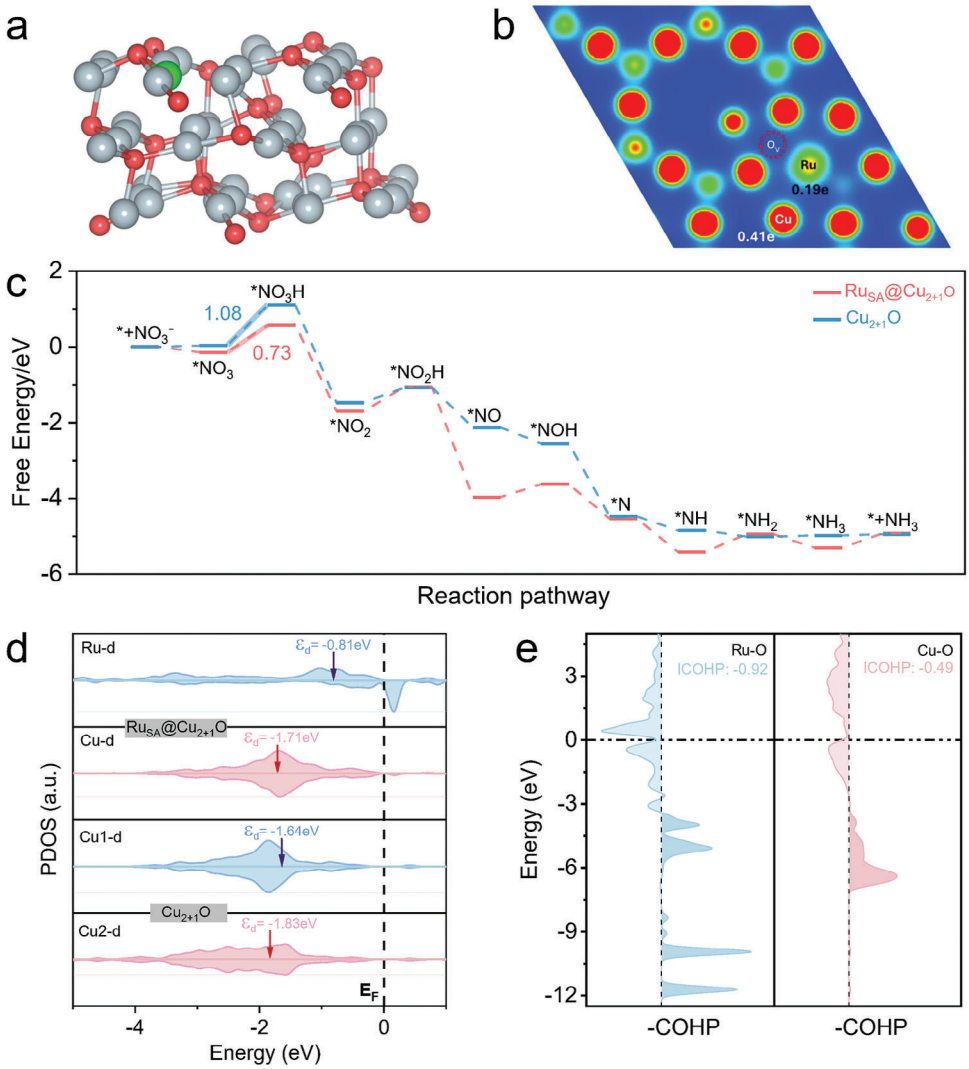

Figure 5. Density functional theory calculation results. a) Theoretical models of $Ru_{SA}@Cu_{2+1}O$ catalyst, in which, grey, red, and green balls represent Cu, O, and Ru atoms. b) 2D charge density distribution of $Ru_{SA}@Cu_{2+1}O$. c) Gibbs free energy diagram for NO_3RR on the $Ru_{SA}@Cu_{2+1}O$ and $Cu_{2+1}O$ catalysts. d) Partial density of states (PDOS) analysis of $Ru_{SA}@Cu_{2+1}O$ and $Cu_{2+1}O$ catalysts. e) Crystal orbital Hamilton population (COHP) evaluations for $^*NO_3$ adsorption on $Ru_{SA}@Cu_{2+1}O$. E_F is set to zero.

As for the $Cu_{2+1}O$ counterpart (Figure S22b,c, Supporting Information), the downward band ≈1629 cm^{-1} correspond to the asymmetric band of NH_2/NO, and the infrared band located at 1115 cm^{-1} can be attributed to the H—N stretching vibration of hydroxylamine (NH_2OH).[1] Simultaneously, several positive bands are observed, including hydrogenation intermediates such as H—N—H at 1435 cm^{-1},[37] NH_2 at 1296 cm^{-1} which produces NH_3 (NH_4^+ at 1450 cm^{-1}).[37] Furthermore, H_2O at 3398 cm^{-1} is attributed to the existence of hydrogen bond association, and the asymmetric band NH+ 4 characteristic peak is focused on 3224 cm^{-1}. Additionally, the infrared vibrational peaks gradually disappear after the applied voltage is removed, indicating the electrocatalytic process derived from the applied potential. Thus, we can conclude that the incorporation of Ru atoms into interphase $Cu_{2+1}O$ lattice can significantly regulate the hydrogenation process of NO_3RR with the accelerated transformation of intermediates.

2.3. Reaction Mechanism Investigated by Theoretical Calculations

In order to get an in-depth understanding of the reaction mechanism, density functional theory (DFT) calculations were performed to gain insights into the catalytic process of NO_3RR on the prepared catalysts. Ru incorporation was introduced into the theoretical $Cu_{2+1}O$ models based on the XAFS findings, and the corresponding stable configurations were defined via structural relaxation and optimization (**Figure 5a**; Figure S23, Supporting Information).[40] The electronic structure of the catalytic sites was first assessed for its crucial role in affecting the catalytic performance. As presented, the asymmetric distribution of the electrons could be found on the catalyst's surfaces, indicating the induced charge polarization (Figure 5b; Figure S24, Supporting Information). Such asymmetric charge distribution was quantifiably substantiated by the Bader charge analysis,

wherein the incorporation of Ru amplifies the charge disparity among active sites, thereby fostering the reaction process.[41,42] The thermodynamics of NO_3RR were then investigated via the Gibbs free energy profile. As illustrated in Figure 5c, it is clear that the potential determining step (PDS) of $Ru_{SA}@Cu_{2+1}O$ and $Cu_{2+1}O$ both located at the first hydrogenation process of $^*NO_3$ ($^*NO_3 \rightarrow ^*NO_3H$), with the energy input of 0.73 and 1.08 eV, respectively (Figures S25 and S26, Supporting Information). The decreased value observed for $Ru_{SA}@Cu_{2+1}O$ catalyst confirmed that the incorporation of Ru atoms effectively lowered the energy barrier of PDS, thus promoting the reduction reaction. To investigate the origin of superior catalytic performance, a density of states analysis of the catalysts was then conducted. As shown in Figure 5d, compared to the pristine $Cu_{2+1}O$ system, the asymmetric charge polarization via the incorporation of Ru atoms brought the d-band center of active sites (Ru and Cu) closer to the Fermi level (E_f), thus increasing the adsorption energy of $^*NO_3$ from -0.43 eV to -0.82 eV (Figure S27, Supporting Information). This adsorption disparity could be intuitively demonstrated by the binding strength of metal—O bonds. Therefore, the bonding and antibonding states of $^*NO_3$ adsorption on the active centers were further evaluated by the crystal orbital Hamilton population (COHP) (Figure 5e, Figure S28, Supporting Information). Quantitative integrated crystal orbital Hamiltonian population (ICOHP) analysis found that the integration value of Ru-O and Cu-O bonding for $Ru_{SA}@Cu_{2+1}O$ catalyst is more negative than the Cu-O for $Cu_{2+1}O$ surface, indicating a stronger binding of $^*NO_3$. These electronic structure observations corroborated that the Ru incorporation could modulate the electronic structures of active sites and the intermediate adsorption strength, thus optimizing the reaction activity. Additionally, to investigate the influence of oxygen vacancies, the catalytic performance of the $Ru_{SA}@Cu_2O$ catalyst without oxygen vacancies was also examined (Figure S29a, Supporting Information). Charge distribution analysis indicates that $Ru_{SA}@Cu_2O$ exhibits inferior charge polarization compared to the $Ru_{SA}@Cu_{2+1}O$ catalyst, with moderate charge disparity among active sites (Figure S29b, Supporting Information). Further simulations of the Gibbs free energy profile found that similar to the $Ru_{SA}@Cu_{2+1}O$ catalyst, the PDS for $Ru_{SA}@Cu_2O$ still occurs during the first hydrogenation process of $^*NO_3$, with an energy barrier of 0.95 eV. This barrier is higher than the value of 0.73 eV for $Ru_{SA}@Cu_{2+1}O$, confirming the role of oxygen vacancy in lowering the catalytic energy barrier (Figure S30, Supporting Information). By comparing the pristine $Cu_{2+1}O$ catalyst (without Ru incorporation), $Ru_{SA}@Cu_2O$ (without oxygen vacancies), and $Ru_{SA}@Cu_{2+1}O$, we can rationally speculate that the integration of oxygen vacancies and Ru incorporation could synergistically optimize the electronic structure of the active sites, thus improving the NO_3RR performance.

2.4. Zn-NO_3^- Battery Application

Since ammonia is a kind of energy carrier with high energy density (4.32 kW h L^{-1}), the Zn-NO- 3 battery is a recently proposed device that integrates both energy generalization and ammonia production in one system, in which the NO_3RR is processed as cathode while Zn dissociation occurs at the anode.[43,44] Hence, constructing high-performance electrode materials toward Zn-NO_3^- battery offers a promising realized application in future water treatment and clean energy generalization. Considering the ideal NO_3RR performance of $Ru_{SA}@Cu_{2+1}O$, it holds great promise for application in novel energy storage and conversion devices. In this work, the Zn-NO_3^- battery was assembled by using $Ru_{SA}@Cu_{2+1}O$ as the cathode and Zn as the anode to evaluate its electrochemical performance (**Figure 6a**).[45–47] As shown in Figure 6b, the open-circuit voltages are 1.318 and 1.271 V versus Zn for $Ru_{SA}@Cu_{2+1}O$ and $Cu_{2+1}O$ assembled batteries, respectively, indicating the potential energy output in future applications. Furthermore, the Zn-NO_3^- battery assembled by $Ru_{SA}@Cu_{2+1}O$ exhibits a higher power density of 9.53 mW cm^{-2} than that of $Cu_{2+1}O$ assembled battery of 6.76 mW cm^{-2}, indicating the higher energy storage capacity of the assembled Zn-NO_3^- battery by $Ru_{SA}@Cu_{2+1}O$. Then, the assembled battery was discharged at various current densities ranging from 2 to 10 mA cm^{-2} to investigate the discharging performance toward Zn-NO_3^- conversion (Figure 6d; Figure S31, Supporting Information), the $Ru_{SA}@Cu_{2+1}O$ assembled battery maintained the initial voltage across these different current densities, consistently returning to the potential corresponding to 2 mA cm^{-2}, which highlights the further application of the battery.[48] Additionally, taking consideration of the advantage of Zn-NO_3^- in energy output along with ammonia production, the ammonia yield was then evaluated at different discharging current densities. As shown in Figure 6e, the ammonia yield increased proportionally with the current density and reached a maximum value of 158.62 mmol h^{-1} cm^{-2} at the discharging current density of 10 mA cm^{-2}. Furthermore, the continuous charging–discharging cycling curves at the current density of 5 mA cm^{-2} underflow battery assembly of $Ru_{SA}@Cu_{2+1}O$ assembled battery show ideal stability, indicating its durability and potential for long-term use in practical applications. This consistent performance over prolonged cycling further supports the viability of the Zn-NO_3^- battery for further application compared to recent reports (Table S5, Supporting Information).

3. Conclusion

In summary, the interphase $Cu_{2+1}O$ with single atom Ru incorporation was first synthesized by fast Joule heating synthesis. Synchrotron radiation-based characterizations demonstrated that the incorporation of Ru significantly regulated the local configuration and the electronic structure of active sites with charge polarizations. The optimized $Ru_{SA}@Cu_{2+1}O$ achieves a maximum FE of 98.02% with an ammonia production rate of 0.81 mmol h^{-1} cm^{-2}. In situ ATR-SEIRAS spectra and theoretical simulations further confirmed that the Ru incorporation promoted the hydrogenation of NO_x, leading to accelerated reaction kinetics. In addition, the Zn-NO- 3 battery uses the $Ru_{SA}@Cu_{2+1}O$ as the cathode achieves a high-power density of 9.53 mW cm^{-2}, with ammonia yield reaches 158.62 mmol h^{-1} cm^{-2}. This work not only introduced a facile approach to fabricate the novel Cu-based catalyst for highly efficient NO_3RR, but also provides insights into the understanding of multi-electron transfer processes.

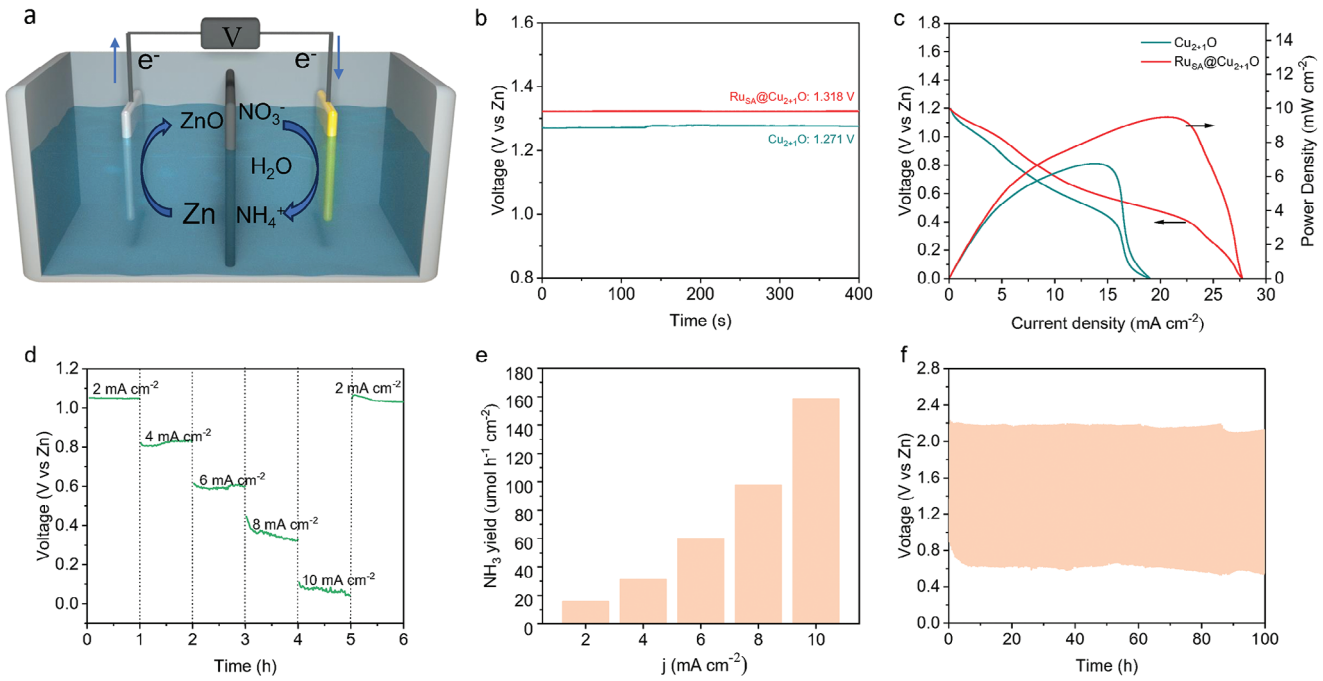

Figure 6. a) Schematic illustration of the Zn-NO_3^- battery, b) OCV measurement of the assembled batteries. c) Polarization and power density curve of the $Ru_{SA}@Cu_{2+1}O$ and $Cu_{2+1}O$ assembled battery. d) Discharging tests at various current densities on $Ru_{SA}@Cu_{2+1}O$ assembled battery. e) Ammonia yield at various discharging current densities for $Ru_{SA}@Cu_{2+1}O$ assembled Zn-NO_3^- battery, f) discharge–charge curves of Zn-NO_3^- battery at 5 mA cm^{-2} at flow battery assembly for $Ru_{SA}@Cu_{2+1}O$.

4. Experimental Section

Synthesis of the Precursor: First, 2 mmol Cu $(NO_3)_2$ and 200 mg $NaBH_4$ were separately dissolved in 10 mL and 5 mL of deionized water, respectively. Subsequently, 500 µL of $RuCl_3$ solution (5 mg mL^{-1}) was added to Cu $(NO_3)_2$ solution (the $Cu_{2+1}O$ does not have this step). Then, the $NaBH_4$ solution was added to the mixture, stirred for 30 min, and centrifuged at 8000 rpm in a high-speed centrifuge for one minute, followed by draining the supernatant. Finally, the mixture was vacuum-dried at 60 °C overnight.

Synthesis of $Cu_{2+1}O$ and $Ru_{SA}@Cu_{2+1}O$ by Fast Joule Heating Synthesis: The precursor was placed in the middle of a carbon cloth and applied in a homemade Joule-heating device equipped with direct current power. The nitrogen gas was selected as the protection gas and continuously injected into the reaction chamber. The voltage was controlled to indirectly regulate the current, promoting rapid heating of the sample at the voltage of 5 V for 20 s.

Synthesis of $Cu_{2+1}O$/CuO under Traditional Tubular Furnace Annealing: Regarding the traditional annealing treatment of the precursor, the precursor was first placed in the middle part of the tubular furnace in a corundum boat. The temperature was raised to 300 °C with a rating of 5 °C min^{-1} and maintained for 3 h by using nitrogen as the protecting gas. After annealing, the temperature was neutrally cooled to room temperature and the product could be obtained.

Electrochemical Measurements: 5 mg of the prepared catalyst was carefully transferred into a 1.5 mL centrifuge tube followed by adding 300 µL of deionized water, 650 µL of ethanol, and 50 µL 5 wt% Nafion solution. The mixture was then subjected to ultrasonic treatment for 30 min to obtain the uniformly dispersed catalyst ink. Subsequently, 50 µL of the catalyst dispersion was absorbed with a pipette and uniformly deposited onto a hydrophilic carbon paper with an area of 1 cm^2 (the catalyst loading was calculated as 0.25 mg cm^{-2}). The working electrode could be obtained after air-drying the carbon paper.

In this work, a traditional three-electrode system was adopted. The working electrode consisted of the catalyst supported by carbon paper, a Hg/HgO electrode was utilized as the reference electrode, and a commercial Pt electrode was employed as the counter electrode. The entire test process was conducted within an H-type electrolytic cell. Prior to the test, 25 mL of electrolyte was poured into both the anode and cathode cells. Subsequently, cyclic voltammetry (CV), LSV, and *I–t*-tests were conducted with the fixed potential range. All potentials recorded during the test were converted to the reversible hydrogen electrode (RHE) scale using the Nernst equation.

$$E\ (\text{V versus RHE}) = E\ (\text{Hg/HgO}) + 0.059 * \text{pH} + 0.098 \quad (1)$$

where E (V vs RHE) is RHE potential after conversion, and E (Hg/HgO) is the actual measured potential using the Hg/HgO electrode.

The ammonia was first determined by UV–vis spectra with an absorption peak near 660 nm, and the ammonia yield was calculated from standard curves with different concentrations. Before testing the ammonia concentration in the electrolyte after each reaction, the concentration of the standard solution was first tested, and then measured the concentration of the post-reaction electrolyte for calculation. Considering the higher ammonia concentration at high reaction voltages, the post-reaction electrolyte was diluted several times using pure electrolyte to ensure that the absorption peak intensity of ammonia falls within the range of the standard curve. The ammonia yield and FE were then calculated by the following formulas:

The NH_3 Faradaic efficiency was calculated according to

$$FE(NH3) = \frac{8*F*C*V}{M*Q} * 100\% \quad (2)$$

The NH_3 yield was calculated according to

$$Y(NH3) = \frac{C*V}{M*t*S} \quad (3)$$

where F is the Faraday's constant (96485 C mol^{-1}), C represents the concentration of NH_3 produced, V is the volume of electrolyte (25 mL), M is the relative molecular mass of NH_3, Q is the applied overall coulomb quantity, t is reaction time (3600 s) and S is reaction area (1 cm^2).

Determination of Ammonia: The concentration of yield ammonia in the electrolyte was detected by indophenol blue indicator through UV–vis absorption spectra. The chromogenic reagent, oxidizing solution, and catalyzing solutions were prepared as follows: Reagent A (Chromogenic reagent): 5 g of sodium salicylate and 5 g potassium sodium tartrate were dissolved into 100 mL of 1 M KOH. Reagent B (Oxidizing solution): 3.5 mL of sodium hypochlorite was added into 100 mL of DI water. Reagent C (Catalyzing solution): 200 mg of sodium nitroferricyanide was dissolved into 20 mL of DI water.

For UV–vis measurements: 2 mL of sample solution was added to the test tube with 2 mL of reagent A, 1 mL of reagent B, and 0.2 mL of reagent C. After shaking up and standing for 1 h, the concentration of the as-prepared sample solution was detected by using UV–vis spectrophotometer.

Determination of NO–2: A total of 5 mL of the electrolyte was added into 100 µL solution containing 2.0 M HCl and 10 mg mL^{-1} sulfanilamide and aging for 10 min. Then, 100 µL of N-(1-Naphthy)ethylenediamine with a concentration of 10 mg mL^{-1} was added into the above solution and standing for another 30 min. The absorbance of NO_2^- was measured by UV–vis spectroscopy at the wavenumber between 450 to 700 nm and the specific absorbance of NO_2^- was at the wavenumber ≈500 nm. The detailed concentration of NO_2^- was calculated by a standard calibration curve obtained by a standard solution of KNO_2.

Zn-NO_3^- Battery Assembly: The Zn-NO_3^- battery was assembled by using the catalysts as the cathode while the polished Zn plate as anode. The typical H-cell containing 30 mL cathode electrolyte of 1 M KOH and 0.1 M KNO_3 and 30 mL anode electrolyte of 1 M KOH separated by Nafion 115 membrane was assembled to evaluate the battery performances. The Zn-NO_3^- battery performance was carried out in the Land CT2001A cell measurements system and CHI760E electrochemical workstation. For flow, the Zn-NO_3^- battery of charging–discharging test was measured by cycling the electrolyte through a peristaltic pump.

Characterizations: Powder X-ray diffraction (XRD) was carried out to characterize samples on a 9 KW advanced X-ray diffractometer equipped with Cu Ka radiation (λ = 1.54178 Å). HRTEM was taken on a JEOL-F200 with an acceleration voltage of 200 kV to obtain the morphology of samples, and corresponding Energy-dispersive X-ray spectroscopy (EDS) mapping analysis. The surface chemical composition and valence states of samples were studied by X-ray photoelectron spectroscopy (XPS, ESCA-LAB250Xi), and the obtained spectra were corrected for specimen charging with C l s binding energy (284.5 eV). The elements molar ratios of the samples were acquired on inductively coupled plasma mass spectrometry (ICP-MS). X-ray absorption fine structure (XAFS) spectra were collected at the beamline BL14W1 in Shanghai Synchrotron Radiation Facility (SSRF) and XMCD endstation of National Synchrotron Radiation Laboratory (NSRL). The synchrotron-radiation Fourier transform infrared spectroscopy was conducted in NSRL at the beamline BL01B.

Theoretical Calculations: Density functional theory (DFT) calculations have been performed to obtain stable geometric structures and electronic properties by using the Vienna ab initio simulation package (VASP).[49,50] The exchange-correlation function was described by the Perdew-Burke-Ernzerhof (PBE) function combined with the generalized gradient approximation (GGA).[51] The projector-augmented wave (PAW) method was applied with a kinetic energy cutoff of 450 eV to describe the expansion of the electronic eigenfunctions.[52] All structures were allowed to relax during the optimization of the geometries until the energy on the atoms was less than 1.0×10^{-5} eV, and the maximal force was converged to 0.01eV $Å^{-1}$ in each degree of freedom for all relaxed atoms. Integration in the first Brillouin zone was approximated via the Monkhorst– Pack grids with the k-points of 3 × 3 × 1. A 2 × 2 supercell of $Cu_{2+1}O$ layer was constructed to model the catalyst substrate. The vacuum thickness was set to 15 Å to minimize interlayer interactions.

For each electron-transfer step, the Gibbs free-energy change (ΔG) can be expressed as follows:

$$\Delta G = \Delta E + \Delta ZPE - T\Delta S \quad (4)$$

wherein, ΔE denotes the energy obtained from DFT calculations. ΔZPE and ΔS are the correction of zero-point energy and entropy, respectively. T represents the room temperature (298.15 K). To avoid calculating the energy of charged NO_3^- directly, gaseous HNO_3 was used as a reference. The adsorption energy of NO_3^- (ΔG_{*NO3}) is described as

$$\Delta G_{*NO3} = G_{*NO3} - G_{*} - G_{HNO3(g)} + 0.5G_{H2(g)} + \Delta G_{correct} \quad (5)$$

where G_{*NO3} is the Gibbs free energy of NO_3^- adsorbed on $Cu_{2+1}O$ substrates, G_{*}, $G_{HNO3(g)}$, and $G_{H2(g)}$ are the free energy $Cu_{2+1}O$ catalyst, HNO_3 and H_2 molecules in the gas phase, respectively. $\Delta G_{correct}$ denotes the correction of adsorption energy which is set to be 0.392 eV.[53]

Supporting Information

Supporting Information is available from the Wiley Online Library or from the author.

Acknowledgements

Y.L., Y.W., and Y.X. contribute equally to this work. This work is financially supported by the National Natural Science Foundation of China (12225508, U23A20121, 12074002, 12205301), National Key Research and Development Program of China (2022YFA1403200), the University Synergy Innovation Program of Anhui Province (GXXT-2023-036), Anhui Provincial Department of Education university natural science research project (2023AH050113, 2024AH050070), the Major Basic Program of Natural Science Foundation of Shandong Province (ZR2021ZD01), Natural Science Foundation of Anhui Province (2208085QB30, 2308085MB47). The authors thank Hefei Advanced Computing Center and the High-Performance Computing Platform of Anhui University for computational support. The authors also thank the Shanghai synchrotron radiation facility (BL14W1, SSRF) and National Synchrotron Radiation Laboratory (Infrared spectroscopy and microspectroscopy, MCD endstation, NSRL) for help in characterizations. The authors acknowledge the Hefei In-situ Technology. Co., Ltd. for experimental help in Joule heating synthesis.

Conflict of Interest

The authors declare no conflict of interest.

Data Availability Statement

The data that support the findings of this study are available from the corresponding author upon reasonable request.

Keywords

$Cu_{2+1}O$, nitrate reduction reaction, synchrotron radiation, XAFS

Received: September 18, 2024
Revised: November 13, 2024
Published online:

[1] S. Han, H. Li, T. Li, F. Chen, R. Yang, Y. Yu, B. Zhang, *Nat. Catal.* **2023**, *6*, 402.
[2] S. Zhang, J. Wu, M. Zheng, X. Jin, Z. Shen, Z. Li, Y. Wang, Q. Wang, X. Wang, H. Wei, J. Zhang, P. Wang, S. Zhang, L. Yu, L. Dong, Q. Zhu, H. Zhang, J. Lu, *Nat. Commun.* **2023**, *14*, 3634.
[3] H. Zhang, H. Wang, X. Cao, M. Chen, Y. Liu, Y. Zhou, M. Huang, L. Xia, Y. Wang, T. Li, D. Zheng, Y. Luo, S. Sun, X. Zhao, X. Sun, *Adv. Mater.* **2024**, *36*, 2312746.
[4] L. Sun, B. Liu, *Adv. Mater.* **2023**, *35*, 2207305.
[5] J. Wang, Y. Wang, C. Cai, Y. Liu, D. Wu, M. Wang, M. Li, X. Wei, M. Shao, M. Gu, *Nano. Lett.* **2023**, *23*, 1897.
[6] K. Yang, S.-H. Han, C. Cheng, C. Guo, T. Li, Y. Yu, *J. Am. Chem. Soc.* **2024**, *146*, 12976.
[7] G. Zhang, X. Li, K. Chen, Y. Guo, D. Ma, K. Chu, *Angew. Chem., Int. Ed.* **2023**, *62*, 202300054.
[8] S. Wang, L. Li, K. San Hui, D. A. Dinh, Z. Lu, Q. Zhang, K. N. Hui, *Nano Energy* **2023**, *113*, 108543.
[9] Y. Wang, A. Xu, Z. Wang, L. Huang, J. Li, F. Li, J. Wicks, M. Luo, D.-H. Nam, C.-S. Tan, Y. Ding, J. Wu, Y. Lum, C.-T. Dinh, D. Sinton, G. Zheng, E. H. Sargent, *J. Am. Chem. Soc.* **2020**, *142*, 5702.
[10] Q. Gao, H. S. Pillai, Y. Huang, S. Liu, Q. Mu, X. Han, Z. Yan, H. Zhou, Q. He, H. Xin, *Nat. Commun.* **2022**, *13*, 2338.
[11] S.-E. Bae, K. L. Stewart, A. A. Gewirth, *J. Am. Chem. Soc.* **2007**, *129*, 10171.
[12] H. Luo, S. Li, Z. Wu, Y. Liu, W. Luo, W. Li, D. Zhang, J. Chen, J. Yang, *Adv. Mater.* **2023**, *35*, 2304695.
[13] J. Xu, S. Zhang, H. Liu, S. Liu, Y. Yuan, Y. Meng, M. Wang, C. Shen, Q. Peng, J. Chen, *Angew. Chem., Int. Ed.* **2023**, *62*, 202308044.
[14] L. Wu, J. Feng, L. Zhang, S. Jia, X. Song, Q. Zhu, X. Kang, X. Xing, X. Sun, B. Han, *Angew. Chem., Int. Ed.* **2023**, *62*, 202307952.
[15] M. Zhang, Z. Ma, S. Zhou, C. Han, V. Kundi, P. V. Kumar, L. Thomsen, B. Johannessen, L. Peng, Y. Shan, *ACS Catal.* **2024**, *14*, 11231.
[16] M. Zheng, Y. Wan, L. Yang, S. Ao, W. Fu, Z. Zhang, Z.-H. Huang, T. Ling, F. Kang, R. Lv, *J. Energy Chem.* **2024**.
[17] J. Ni, J. Yan, F. Li, H. Qi, Q. Xu, C. Su, L. Sun, H. Sun, J. Ding, B. Liu, *Adv. Energy Mater.* **2024**, *14*, 2400065.
[18] Y. Yao, L. Zhao, J. Dai, J. Wang, C. Fang, G. Zhan, Q. Zheng, W. Hou, L. Zhang, *Angew. Chem., Int. Ed.* **2022**, *61*, 202208215.
[19] L. Bai, F. Franco, J. Timoshenko, C. Rettenmaier, F. Scholten, H. S. Jeon, A. Yoon, M. Rüscher, A. Herzog, F. T. Haase, S. Kühl, W. Chee, See, A. B., R. C. Beatriz, *J. Am. Chem. Soc.* **2024**, *146*, 9665.
[20] S. Paul, S. Sarkar, A. Adalder, S. Kapse, R. Thapa, U. K. Ghorai, *ACS Sustainable Chem. Eng.* **2023**, *11*, 6191.
[21] A. Adalder, S. Paul, N. Barman, A. Bera, S. Sarkar, N. Mukherjee, R. Thapa, U. K. Ghorai, *ACS Catal.* **2023**, *13*, 13516.
[22] N. Mukherjee, A. Adalder, N. Barman, R. Thapa, R. Urkude, B. Ghosh, U. K. Ghorai, *J. Mater. Chem. A* **2024**, *12*, 3352.
[23] S. Sarkar, A. Adalder, S. Paul, S. Kapse, R. Thapa, U. K. Ghorai, *Appl. Catal. B: Environ.* **2024**, *343*, 123580.
[24] Y. Li, Y. K. Go, H. Ooka, D. He, F. Jin, S. H. Kim, R. Nakamura, *Angew. Chem., Int. Ed.* **2020**, *59*, 9744.
[25] D. F. Abbott, Y. Z. Xu, D. A. Kuznetsov, P. Kumar, C. R. Müller, A. Fedorov, V. Mougel, *Angew. Chem.* **2023**, *135*, 202313746.
[26] D. F. Abbott, Y. Z. Xu, D. A. Kuznetsov, P. Kumar, C. R. Müller, A. Fedorov, V. Mougel, *Angew. Chem.* **2023**, *62*, 202313746.
[27] J. Yang, H. Qi, A. Li, X. Liu, X. Yang, S. Zhang, Q. Zhao, Q. Jiang, Y. Su, L. Zhang, *J. Am. Chem. Soc.* **2022**, *144*, 12062.
[28] X. Li, Y. Chen, X. Zhan, Y. Xu, L. Hao, L. Xu, X. Li, M. Umer, X. Tan, B. Han, *The Innovation Materials* **2023**, *1*, 100014.
[29] Y. Wang, M. m. Shi, D. Bao, F. l. Meng, Q. Zhang, Y. t. Zhou, K. h. Liu, Y. Zhang, J. z. Wang, Z. w. Chen, *Angew. Chem.* **2019**, *131*, 9564.
[30] Z. Gu, Y. Zhang, X. Wei, Z. Duan, Q. Gong, K. Luo, *Adv. Mater.* **2023**, *35*, 2303107.
[31] B. Zhang, Z. Dai, Y. Chen, M. Cheng, H. Zhang, P. Feng, B. Ke, Y. Zhang, G. Zhang, *Nat. Commun.* **2024**, *15*, 2816.
[32] L. Qu, S. Kim, R. Tan, A. Sivanantham, S. Kim, Y. J. Jeong, M. C. Kim, S. S. Shin, U. Sim, I. S. Cho, *J. Energy Chem.* **2024**, *99*, 475.
[33] H. Zhu, S. Dong, X. Du, H. Du, J. Xia, Q. Liu, Y. Luo, H. Guo, T. Li, *Catal. Sci. Tech.* **2022**, *12*, 4998.
[34] J. R. Deka, D. Saikia, K. S. Hsia, H. M. Kao, C. S. Chen, *Catalysts* **2020**, *10*, 267.
[35] Z. Wang, R. Lin, Y. Huo, H. Li, L. Wang, *Adv. Funct. Mater.* **2022**, *32*, 2109503.
[36] Z. Gu, Y. Zhang, Y. Fu, D. Hu, F. Peng, Y. Tang, H. Yang, *Angew. Chem., Int. Ed.* **2024**, 202409125.
[37] K. Chen, Y. Zhang, X. Z. Jiaqi Xiang, X. Li, a. K. Chu, *ACS Energy Lett.* **2023**, *8*, 1281.
[38] J.-Y. Fang, Q.-Z. Zheng, Y.-Y. Lou, K.-M. Zhao, S.-N. Hu, G. Li, O. Akdim, X.-Y. Huang, S.-G. Sun, *Nat. Commun.* **2022**, *13*, 7899.
[39] X. Li, P. Shen, X. Li, D. Ma, K. Chu, *ACS Nano* **2023**, *17*, 1081.
[40] H. Wang, R. Sun, P. Liu, H. Hu, C. Ling, X. Han, Y. Shi, X. Zheng, G. Wu, X. Hong, *Nano Res.* **2024**, *17*, 7013.
[41] J. Xu, X.-X. Xue, G. Shao, C. Jing, S. Dai, K. He, P. Jia, S. Wang, Y. Yuan, J. Luo, *Nat. Commun.* **2023**, *14*, 7849.
[42] L. H. Zhang, Y. Jia, J. Zhan, G. Liu, G. Liu, F. Li, F. Yu, *Angew. Chem., Int. Ed.* **2023**, *62*, 202303483.
[43] Y. Wang, F. Hao, M. Sun, M. T. Liu, J. Zhou, Y. Xiong, C. Ye, X. Wang, F. Liu, J. Wang, P. Lu, Y. Ma, J. Yin, H.-C. Chen, Q. Zhang, L. Gu, H. Chen, B. Huang, Z. Fan, *Adv. Mater.* **2024**, *36*, 2313548.
[44] R. Zhang, C. Li, H. Cui, Y. Wang, S. Zhang, P. Li, Y. Hou, Y. Guo, G. Liang, Z. Huang, C. Peng, C. Zhi, *Nat. Commun.* **2023**, *14*, 8036.
[45] R. Zhang, Y. Guo, S. Zhang, D. Chen, Y. Zhao, Z. Huang, L. Ma, P. Li, Q. Yang, G. Liang, *Adv. Energy Mater.* **2022**, *12*, 2103872.
[46] H. Jiang, G. F. Chen, O. Savateev, J. Xue, L. X. Ding, Z. Liang, M. Antonietti, H. Wang, *Angew. Chem., Int. Ed.* **2023**, *62*, 202218717.
[47] L. Zhou, X. Chen, S. Zhu, K. You, Z. J. Wang, R. Fan, J. Li, Y. Yuan, X. Wang, J. Wang, *Angew. Chem.* **2024**, *136*, 202401924.
[48] Y. Lee, J. Theerthagiri, N. Yodsin, A. Min, C. J. Moon, S. Jungsuttiwong, M. Y. Choi, *Angew. Chem., Int. Ed.* 202413774.
[49] G. Kresse, J. Furthmüller, *Phys. Rev. B* **1996**, *54*, 11169.
[50] G. Kresse, D. Joubert, *Phys. Rev. B* **1999**, *59*, 1758.
[51] J. P. Perdew, K. Burke, M. Ernzerhof, *Phys. Rev. Lett.* **1996**, *77*, 3865.
[52] P. E. Blöchl, *Phys. Rev. B* **1994**, *50*, 17953.
[53] J.-X. Liu, D. Richards, N. Singh, B. R. Goldsmith, *ACS Catal.* **2019**, *9*, 7052.